










Efficient computation of blood velocity in the left atrial appendage: A practical perspective


Audrius Aidietis^{a, b} , Sigita Aidietienė^{a, b} , Oleg Ardatov^c ,
Sergejus Borodinas^d , Rimgaudas Katkus^{a, b}, Kristina Kaulakytė^{e, 1} ,
Nikolajus Kozulinas^e , Grigory Panasenko^{e, f, 2} , Konstantinas Pileckas^{e, 3} ,
Gediminas Račkauskas^{a, b} 

^a Vilnius University Hospital Santaros Klinikos, Lithuania 

^b Centre for Cardiology and Angiology, Department of Cardiovascular Diseases,
Faculty of Medicine, Vilnius University, Lithuania 

^c Faculty of Mechanics, Vilnius TECH, Lithuania 

^d Faculty of Civil Engineering, Vilnius TECH, Lithuania 

^e Faculty of Mathematics and Informatics, Vilnius University, Lithuania 

^f Institute Camille Jordan UMR CNRS 5208, University Jean Monnet, 
St. Etienne, France
grigory.panasenko@univ-st-etienne.fr

Received: October 2, 2024 / **Revised:** August 19, 2025 / **Published online:** October 7, 2025

Abstract. The goal of the paper is to present the FSI (fluid-structure interaction) CFD (computational fluid dynamics) simulations of the blood flow in the LA (left atrium) for patient-specific geometry of the left atrium appendage (LAA). These simulations are important for the decision making in cardiology and cardiac surgery of the patients with atrial fibrillation. Nowadays according current atrial fibrillation treatment guidelines, initiation of oral anticoagulant therapy is recommended for patients with a CHA₂DS₂–VASc score greater or equal to 2 for males, and greater or equal to 3 for females, for lowering stroke risk. This therapy although has undesirable effects and provokes bleeding in a part of cases. That is why it is important to detect the stagnation zones of the blood flow in LAA. The presence of such zones justifies the necessity of the anticoagulant therapy.

The FSI CFD simulations in the heart is a challenging problem: the existing softwares are not too robust for real life Reynolds numbers and often do not converge to the solution of the Navier–Stokes equations for the blood coupled with the elasticity equations of the wall. That is why we first provide the CFD computations with the rigid wall when the codes are more stable. Using this solution as a source of parameters for the implicit numerical scheme solver, we then provide the FSI computations, which become much more robust.

Keywords: Navier–Stokes equations, fluid structure interaction, mathematical modeling, computer simulations.

^{1, 2, 3} The author's research was supported by the Research Council of Lithuania (LMTLT), agreement No. S-MIP-24-54.

1 Introduction

Circulatory diseases are the leading causes of death in the world [5]. These diseases are mostly related to the thrombus formation in various parts of the circulatory system [5]. One of the most dangerous scenarios is thrombogenesis at the left atrium appendage (LAA) of the heart during the atrial fibrillation (AF). The choice of the treatment strategy needs the detailed patient-specific information on the blood circulation in LAA. The information obtained by the clinical investigations of a patient by MRI, CT, or ECG technique is not complete, that is why the modern clinical practice uses some scores; see, for example, Table 1. Such scores are not too reliable. That is why actually mathematical modeling becomes an important tool to get much more precise information on the blood flow in patient-specific LAA and to evaluate the thrombogenesis risk. Two main directions are developed in this context: the first one is the direct computer simulations of the blood flow in patient-specific LAA with detection of stagnation zones as the probable places of thrombogenesis; while the second one is related to the detailed mathematical modeling of the coagulation process (coagulation cascade of reactions) combined with the hemodynamics; see [1, 3, 6, 7, 10, 13, 18–23, 26, 27]. The second direction allows to understand the physiological mechanism of thrombogenesis but it needs the characterization of multiple parameters regarding the reaction kinetics, which is difficult to obtain in clinical practice; also the models are sensitive to uncertainties in these parameters. The main challenges in the first direction are fluid dynamics simulations in patient-specific (not idealized) complex geometry, which is in reality time dependent due to the heart-wall motion; see [2, 8, 11, 14, 24, 25]. Thus, in recent paper [25], LA is modelled by a very simplified geometry, [2] simulates the flow in LA with rigid (not moving) wall.

The approach presented below differs from the cited papers on LAA simulations by taking into consideration of both solid and fluid mechanics descriptions in the frame of the FSI model. This approach allows to compute the blood flow velocity in LAA with the moving wall and eventually provide the stress-strain analysis of the heart wall.

In the present article, we introduce a fluid-structure interaction (FSI) model of the blood flow in the left atrium (LA) and provide two patient-specific studies of the stagnation zones. One of the patients had a stroke and the second did not. We will also discuss the challenges of the FSI simulations such as convergence of the numerical process. The

Table 1. CHA₂DS₂–VASc (or CHADS₂) score system. Maximum total score = 10 points. Anticoagulation recommendations: score = 0 no therapy; score ≥ 2 oral anticoagulation; see [15].

		CHA ₂ DS ₂ –VASc score
C	Congestive heart failure	1 point
H	Hypertension	1 point
A ₂	Age ≥ 75 years	2 points
D	Diabetes	1 point
S ₂	Stroke	2 points
V	Vascular disease	1 point
A	Age ≥ 65 years	1 point
Sc	Sex category, female	1 point

research starts from computed tomography (CT) imaging, segmentation, cleaning (noise reduction), and subsequent domain generation. The obtained domain is then employed to solve the Navier–Stokes equations within the LA, accounting for the elastic behavior of the LA wall. By applying the FSI model we computed the velocity and the pressure in the LA, and in particular, in the LAA. The contraction of the LA is simulated by the application of the outer pressure. The model was validated for the contraction force by controlling the 20% decreasing of the volume of the LA, for the inflow-outflow boundary conditions by comparing the computed velocity with the measured by Doppler technique velocity at some points in LA (note that measurement of the velocity inside the LAA is very difficult).

1.1 Short introduction to the LAA classification

The human heart comprises four chambers: the Left Atrium, Left Ventricle, Right Atrium, and Right Ventricle. LA is equipped with an appendage known as the Left Atrial Appendage. In case of dysfunction called Atrial Fibrillation (AF), the probability of thrombi formation increases, leading to a heightened risk of cardioembolic events.

The length of the LAA is on average 45 mm long with a range from 27 to 60 mm. The types of LAA in the paper [4] are classified into the following geometries: “chicken wing” (48% of population), “windsock” (19% of population), “cauliflower” (3% of population), and “cactus” (30% of population).

During normal sinus rhythm, the risk of a thrombus formation is very low (see [12]), but during AF, it is much higher. It can be explained by the fact that the blood flow velocity, which results from a combination of LAA contraction and filling, is much lower when compared to sinus rhythm.

1.2 Imaging. Cleaning. Making geometry

The imaging process involved a chest Computed Tomography (CT) scans, which come in Digital Imaging and Communications in Medicine (DICOM) format files. One such file consists of a set of images with headers. In the case of a CT scan of the heart, the file includes images of about 500 slices of the human chest. Figure 1 shows one of the slices of a CT scan opened in 3D-Slicer software, used for visualizing and processing 3D images. The images, viewed in three planes (the axial, sagittal, and coronal) were manually segmented to separate the left side of the heart from surrounding tissues. 3D-Slicer produced a primary geometry of the left side of the heart with a rough surface and parts of veins that were unnecessary for the calculations, and therefore removed. The resulting .stl file was edited using Meshlab, a software for processing 3D triangular meshes. The rough surface of the primary geometry would have up to 300000 triangular elements. To simplify the process of editing the geometry, the number of mesh elements was reduced to 30000 elements.

SolidWorks2022 was then used to edit the .ply file. This software is used to design, analyse, and visualize models of solid objects. The left ventricle and parts of the pulmonary veins that extended the most were removed, and mesh errors (such as inverted



Figure 1. CT of a human chest area.

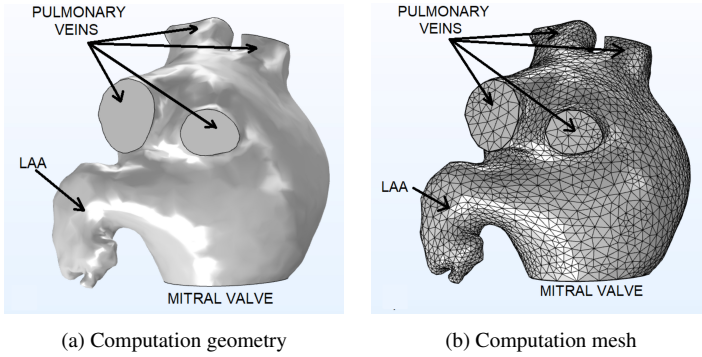


Figure 2. Left Atrium (LA) containing Left Atrial Appendage (LAA).

mesh elements and very fine elements pointing outwards) were avoided. The surface was smoothened so that the model would upload to COMSOL and the calculations would converge, but the geometry remained as close to the original left atrium as possible; see Fig. 2.

1.3 Formulation of the problem

The present section gives the detailed mathematical formulation of the model. Further in the Appendix, we describe the choice of modules and options in the COMSOL software implementing this mathematical model.

The model considers the four pulmonary veins as inlets and the mitral valve as the outlet. The whole interior part of the LA is considered as a fluid domain G ; see Fig. 2(a). We use the FSI model. The boundary of domain G is presented as a union of three parts: the lateral wall of the LA (fluid-structure interface), denoted as Γ_1 , four cross-sections $\gamma_2^{(1)}, \dots, \gamma_2^{(4)}$ of the pulmonary veins (we denote $\Gamma_2 = \cup_{i=1}^4 \gamma_2^{(i)}$), and the mitral zone cross-section Γ_3 ; see Fig. 3. The wall is considered as a thin elastic layer (shell) denoted G_d , where d is a thickness of the shell. At rest, it occupies the space between surfaces Γ_1 and $\Gamma_{1,d}$ at the distance d from Γ_1 in the direction of the outer normal vector. The

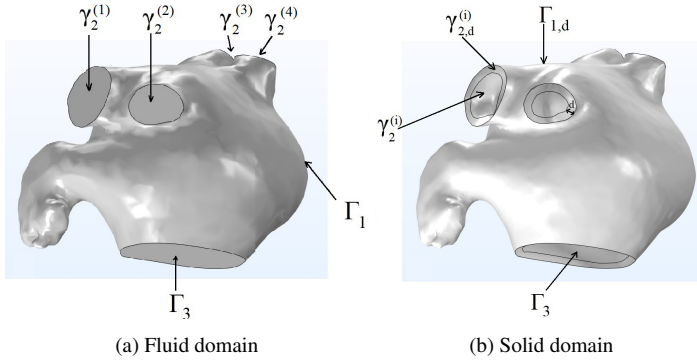


Figure 3. Four pulmonary veins (inlets), mitral valve (outlet) domains, and boundaries of geometry.

lateral boundary of the wall $\partial G_d \setminus (\Gamma_1 \cup \Gamma_{1,d})$ is perpendicular to Γ_1 and consists of five components. Four of them correspond to the cross-sections of the vein walls and are denoted $\gamma_{2,d}^{(1)}, \dots, \gamma_{2,d}^{(4)}$. The fifth corresponds to Γ_3 and is denoted $\gamma_{3,d}$.

The elastic wall moves, and so Γ_1 also moves. The fluid motion equations are set in the time dependent domain G^t between the current in time position of the wall, Γ_2 and Γ_3 . The current position of the wall is characterized by the unknown displacement vector $\mathbf{u}(x, t)$, where $x \in G_d$, so that the moving part of the boundary is $\Gamma_1^t = \{x + \mathbf{u}(x, t), x \in \Gamma_1\}$. The equations determining displacements $\mathbf{u}(x, t)$ in the elastic wall are defined further.

The blood flow in the LA (domain G^t) is described by the Navier–Stokes equations

$$\begin{aligned} \rho_f \mathbf{v}_t - \mu_f \Delta \mathbf{v} + \rho_f (\mathbf{v} \cdot \nabla) \mathbf{v} + \nabla p &= 0, \\ \operatorname{div} \mathbf{v} &= 0, \end{aligned} \quad (1)$$

where \mathbf{v} is the blood velocity, p is the pressure function, $\rho_f > 0$ is the density of the blood, and $\mu_f > 0$ is the constant dynamic viscosity of the blood, with the initial condition

$$\mathbf{v}(x, 0) = 0 \quad (2)$$

and boundary or interface conditions on Γ_1 , Γ_2 , and Γ_3 , which will be described below.

On Γ_2 , the inflow boundary conditions are introduced as the given velocity

$$\mathbf{v}(x, t)|_{\Gamma_2} = \mathbf{g}(x, t), \quad (3)$$

where on each component $\gamma_2^{(i)}$ of Γ_2 , function \mathbf{g} is defined as follows. The inlet flow boundary conditions correspond to the given nonstationary Poiseuille velocity. However, in reality the inlet velocity is unknown. Instead, we know the inlet average velocity $F(t)$ and the total inlet flux $\Phi(t)$ (it is equal to the product of average velocity by the area of the inlet cross-sections). The nonstationary Poiseuille velocities for each inlet cross-section $\gamma_2^{(i)}$, $i = 1, 2, 3, 4$, then can be computed as the solution of an inverse heat problem in an infinite tube with the cross-section $\gamma_2^{(i)}$, where the right-hand side q of the heat equation

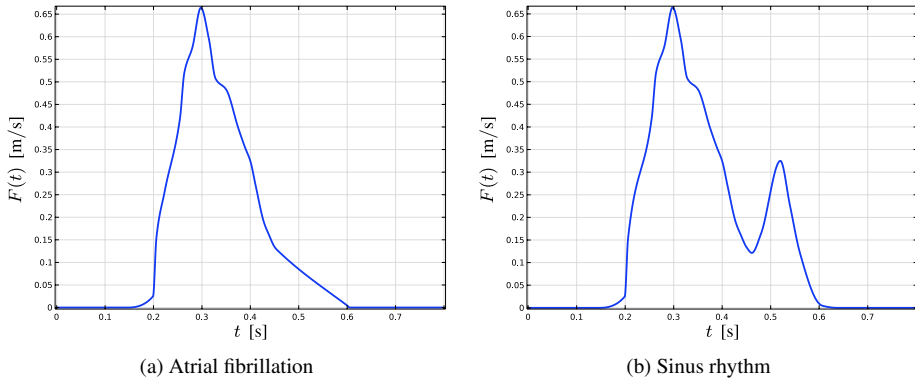


Figure 4. Inlet average velocity $F(t)$.

is the unknown pressure slope, while the total inlet flux Φ is a given function, which is distributed in four parts proportionally to the area of the cross sections $\gamma_2^{(i)}$, $i = 1, 2, 3, 4$. This inverse problem appears as a direct consequence of the Navier–Stokes equations written in the tube under the Poiseuille flow hypothesis that the tangential velocities are equal to zero, while the normal velocity does not depend on the normal variable, and the pressure is a linear function depending on the normal variable with the slope $q(t)$. Namely, this inverse problem has the following form.

Let \tilde{x}_1, \tilde{x}_2 be the local in-plane coordinates of $\gamma_2^{(i)}$, and let $v_{P,i}(\tilde{x}_1, \tilde{x}_2, t), q(t)$ be the solution of the inverse heat problem set on $\gamma_2^{(i)} \times (0, +\infty)$

$$\begin{aligned} \rho_f \frac{\partial v_{P,i}}{\partial t}(\tilde{x}_1, \tilde{x}_2, t) - \mu_f \Delta v_{P,i}(\tilde{x}_1, \tilde{x}_2, t) &= q(t), \\ v_{P,i}|_{\partial\gamma_2^{(i)}} &= 0, \quad v_{P,i}|_{t=0} = 0, \\ \int_{\gamma_2^{(i)}} v_{P,j}(\tilde{x}_1, \tilde{x}_2, t) d\tilde{x}_1 d\tilde{x}_2 &= \Phi(t) \frac{\text{mes } \gamma_2^{(i)}}{\sum_{j=1}^4 \text{mes } \gamma_2^{(j)}} \end{aligned}$$

with $\Phi(t)$ standing for the total inlet flux; see [16, 17].

The tangential components of \mathbf{g} are equal to zero, while the normal component $g_n(\tilde{x}_1, \tilde{x}_2, t)$ on $\gamma_2^{(i)}$ is defined as

$$g_n(\tilde{x}_1, \tilde{x}_2, t) = v_{P,i}(\tilde{x}_1, \tilde{x}_2, t).$$

Such structure of the inflow velocity corresponds to the nonstationary Poiseuille flow corresponding to the given flux depending on time. It corresponds to the flow in an infinite tube with cross-section $\gamma_2^{(i)}$. So, these inflows approximate the blood coming to the inlets through some cylinders modeling the pulmonary veins. In this case, the average velocity (flux divided by the cross section area) is the same for all four inlet cross-sections and is equal to $F(t)$ introduced by the graph at Fig. 4. Here $F(t) = \Phi(t) (\sum_{j=1}^4 \text{mes } \gamma_2^{(j)})^{-1}$.

On Γ_3 , the outflow boundary conditions are introduced as follows:

$$\mathbf{v}_\tau(x, t)|_{\Gamma_3} = 0, \quad p(x, t)|_{\Gamma_3} = 0. \quad (4)$$

Here \mathbf{v}_τ is the tangential velocity at the boundary. The boundary condition $p(x, t)|_{\Gamma_3} = 0$ follows from a more general condition that the normal component of the normal stress is equal to zero:

$$(-pI + \mu_f(\nabla \mathbf{v} + (\nabla \mathbf{v})^T)) \mathbf{n} \cdot \mathbf{n} = 0.$$

Taking into account the equation $\operatorname{div} \mathbf{v} = \mathbf{0}$ and condition $\mathbf{v}_\tau = 0$, we derive that $p = 0$ on Γ_3 .

The part Γ_1 of the boundary ∂G is the interface between the fluid and the elastic solid. The wall corresponding myocardium is described by the nonlinear elasticity equations for the unknown displacement $\mathbf{u}(x, t)$, where $x \in G_d$:

$$\rho \frac{\partial^2 \mathbf{u}}{\partial t^2}(x, t) - \nabla \cdot (J \sigma \mathbf{F}^{-T})^T = 0.$$

Here $\rho > 0$ is the density of the wall material, $\mathbf{F} = I + \nabla \mathbf{u}$ is the deformation gradient, $J \sigma \mathbf{F}^{-T}$ is the 1st Piola–Kirchhoff stress, $J = \det \mathbf{F}$ is the Jacobian determinant, and σ_{ij} is the stress tensor satisfying the linear Hooke's law:

$$\sigma_{ij} = \lambda \sum_{k=1}^3 \varepsilon_{kk} \delta_{ij} + 2\mu \varepsilon_{ij},$$

where λ and μ are the Lamé parameters, δ_{ij} is the Kronecker's delta:

$$\delta_{ij} = \begin{cases} 0 & \text{if } i \neq j, \\ 1 & \text{if } i = j, \end{cases}$$

while

$$\varepsilon_{ij} = \frac{1}{2} \left(\frac{\partial u_i}{\partial x_j} + \frac{\partial u_j}{\partial x_i} + \sum_{k=1}^3 \frac{\partial u_k}{\partial x_i} \frac{\partial u_k}{\partial x_j} \right)$$

is the strain tensor. In the linear theory, it is linearized as

$$\varepsilon_{ij} = \frac{1}{2} \left(\frac{\partial u_i}{\partial x_j} + \frac{\partial u_j}{\partial x_i} \right).$$

Note that the Lamé constants can be expressed via the Young modulus E and the Poisson ratio ν , $E > 0$, $-1 < \nu < 1/2$:

$$\lambda = \frac{E\nu}{(1+\nu)(1-2\nu)}, \quad \mu = \frac{E}{2(1+\nu)}.$$

This system of equations necessitates two initial conditions for \mathbf{u}

$$\mathbf{u}(x, 0) = 0, \quad \frac{\partial \mathbf{u}}{\partial t}(x, 0) = 0, \quad x \in G_d,$$

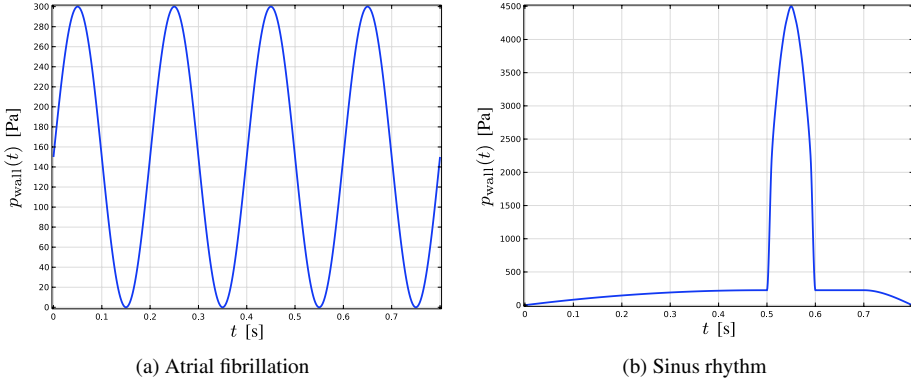


Figure 5. Pressure load $p_{\text{wall}}(t)$ on the shell.

boundary conditions on $\partial G_d \setminus (\Gamma_1 \cup \Gamma_{1,d})$ (clamped ends)

$$\mathbf{u}(x, t) = 0, \quad x \in \partial G_d \setminus (\Gamma_1 \cup \Gamma_{1,d}),$$

boundary condition on $\Gamma_{1,d}$ (applied pressure $p_{\text{wall}}(t)$ simulating the contractions of the wall displayed in Fig. 5)

$$(J\sigma \mathbf{F}^{-T})^T \mathbf{n} = -p_{\text{wall}}(t)\mathbf{n}, \quad x \in \Gamma_{1,d},$$

and, finally, the junction conditions on the moving interface Γ_1 : the continuity of the velocity at the moving interface

$$\mathbf{v}(x + \mathbf{u}(x, t), t) = \frac{\partial \mathbf{u}}{\partial t}(x, t), \quad x \in \Gamma_1$$

and the continuity of the stresses

$$-(J\sigma \mathbf{F}^{-T})^T \mathbf{n} = (-pI + \mu_f(\nabla \mathbf{v} + (\nabla \mathbf{v})^T))\mathbf{n}, \quad x \in \Gamma_1,$$

\mathbf{u} is an outer normal for G . As before, we can replace the right-hand side of this condition by $-p\mathbf{n}$.

The parameters of the model are taken as follows: $d = 2.5 \cdot 10^{-3}$ m, $\rho_f = \rho = 1050$ kg/m³, $\mu_f = 3.5 \cdot 10^{-3}$ Pa·s, $\nu = 0.47$, E belongs to the interval $[4 \cdot 10^4, 8 \cdot 10^5]$ Pa. We considered the Young modulus depending on time, following the contraction pressure $p_{\text{wall}}(t)$ graph

$$E(t) = 4 \cdot 10^4 + p_{\text{wall}}(t) \frac{8 \cdot 10^5 - 4 \cdot 10^4}{\max p_{\text{wall}}},$$

i.e. strengthening when the heart wall muscles contract; see [9].

The necessity of the geometrically nonlinear elasticity model for the description of three-dimensional solid part is motivated by large displacements of the heart wall in the

case of sinus rhythm regime. It also allows to compute more accurate nonlinear strains and stresses in the heart wall to model eventually risks of rupture of the heart muscle. The COMSOL computations use the dimension reduction of this model in the solid part, the so called Uflyand–Mindlin approximation. There are several versions of this approximation, so that in the next section, we will describe the version used in computations.

1.4 Uflyand–Mindlin shell approximation

To solve this problem numerically we used the COMSOL software. The thin layer G_d was approximated by the Uflyand–Mindlin shell model. According to the Uflyand–Mindlin shell theory, the displacement vector \mathbf{u} is supposed to have the following form:

$$\mathbf{u}(\tilde{x}_1, \tilde{x}_2, \tilde{x}_3, t) = \boldsymbol{\eta}(\tilde{x}_1, \tilde{x}_2, t) + \tilde{x}_3 \boldsymbol{\zeta}(\tilde{x}_1, \tilde{x}_2, t), \quad (5)$$

where \tilde{x}_1 and \tilde{x}_2 are the in-plane local coordinates of the shell, $\tilde{x}_3 \in [-d/2, d/2]$ is the normal coordinate, equal to zero on the mid-surface $\Gamma_{1,d/2}$ (at the distance $d/2$ from Γ_1 and from $\Gamma_{1,d}$, see Fig. 6), $\boldsymbol{\eta}(\tilde{x}_1, \tilde{x}_2, t)$ is the displacement vector of the mid-surface of the shell, and $\boldsymbol{\zeta}(\tilde{x}_1, \tilde{x}_2, t)$ is the angular displacement of shell normal ($\boldsymbol{\zeta} \cdot \mathbf{n} = 0$). Further, for the shell equations theory, $\Gamma_{1,d/2}$ is replaced (approximated) by Γ_1 .

The first condition at the interface is the continuity of the velocity on moving boundary:

$$\mathbf{v}(x + \boldsymbol{\eta}(\tilde{x}_1, \tilde{x}_2, t), t) = \frac{\partial \boldsymbol{\eta}}{\partial t}(\tilde{x}_1, \tilde{x}_2, t).$$

The second condition relates the unknown functions $\boldsymbol{\eta}$, $\boldsymbol{\zeta}$ and the pressure p by the system of equations of motion of the shell. This system consists of two equations corresponding to the second-order time derivatives of $\boldsymbol{\eta}$, $\boldsymbol{\zeta}$ in the left-hand side. To get these equations at some point \tilde{x} of the interface Γ_1 , let us expand the expression $\nabla \cdot ((J\sigma \mathbf{F}^{-T})^T)$ with $\mathbf{u}(\tilde{x}_1, \tilde{x}_2, \tilde{x}_3, t)$ replaced by the sum (5) according to the first-order Taylor's formula with respect to the normal variable \tilde{x}_3 :

$$\nabla \cdot ((J\sigma \mathbf{F}^{-T})^T) = \boldsymbol{\Phi}[\boldsymbol{\eta}, \boldsymbol{\zeta}](\tilde{x}_1, \tilde{x}_2, t) + \tilde{x}_3 \boldsymbol{\Psi}[\boldsymbol{\eta}, \boldsymbol{\zeta}](\tilde{x}_1, \tilde{x}_2, t) + o(\tilde{x}_3),$$

where $\boldsymbol{\Phi}[\boldsymbol{\eta}, \boldsymbol{\zeta}]$, $\boldsymbol{\Psi}[\boldsymbol{\eta}, \boldsymbol{\zeta}]$ are expressions containing functions $\boldsymbol{\eta}$, $\boldsymbol{\zeta}$ and their space derivatives of order one and two. Then the second condition has the following form:

$$\begin{aligned} \rho \frac{\partial^2 \boldsymbol{\eta}}{\partial t^2}(\tilde{x}_1, \tilde{x}_2, t) &= \boldsymbol{\Phi}[\boldsymbol{\eta}, \boldsymbol{\zeta}](\tilde{x}_1, \tilde{x}_2, t) + d^{-1}(-p_{\text{wall}} + p)\mathbf{n}, \\ \rho \frac{\partial^2 \boldsymbol{\zeta}}{\partial t^2}(\tilde{x}_1, \tilde{x}_2, t) &= \boldsymbol{\Psi}[\boldsymbol{\eta}, \boldsymbol{\zeta}](\tilde{x}_1, \tilde{x}_2, t). \end{aligned}$$

The first equation here corresponds to the force balance. The second one corresponds to the momentum balance.

The initial conditions for the shell are:

$$\begin{aligned} \boldsymbol{\eta}(\tilde{x}_1, \tilde{x}_2, 0) &= 0, \quad \frac{\partial \boldsymbol{\eta}}{\partial t}(\tilde{x}_1, \tilde{x}_2, 0) = 0, \quad \tilde{x}_1, \tilde{x}_2 \in \Gamma_1, \\ \boldsymbol{\zeta}(\tilde{x}_1, \tilde{x}_2, 0) &= 0, \quad \frac{\partial \boldsymbol{\zeta}}{\partial t}(\tilde{x}_1, \tilde{x}_2, 0) = 0, \quad \tilde{x}_1, \tilde{x}_2 \in \Gamma_1. \end{aligned}$$

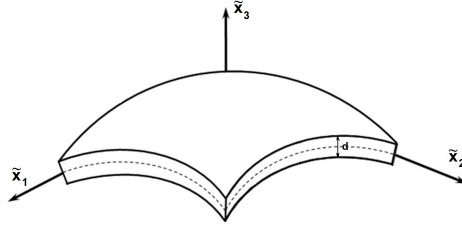


Figure 6. Local coordinates for shell.

The boundary conditions for the shell are chosen as follows:

$$\begin{aligned} \eta(\tilde{x}_1, \tilde{x}_2, t) &= 0, \quad \zeta(\tilde{x}_1, \tilde{x}_2, t) = 0, \quad \tilde{x}_1, \tilde{x}_2 \in \partial\Gamma_2 \\ \eta(\tilde{x}_1, \tilde{x}_2, t) &= 0, \quad M_{nn}(\tilde{x}_1, \tilde{x}_2, t) = 0, \quad M_{n\tau}(\tilde{x}_1, \tilde{x}_2, t) = 0, \quad \tilde{x}_1, \tilde{x}_2 \in \partial\Gamma_3, \end{aligned}$$

where M_{nn} is the normal moment at the boundary of Γ_3 , while τ is the tangential direction (for example, if x_1 is the normal direction, then $M_{11}(\tilde{x}_1, \tilde{x}_2, t) = 0, M_{21}(\tilde{x}_1, \tilde{x}_2, t) = 0$).

Here the moments are defined as $M = \int_{-d/2}^{d/2} \tilde{x}_3 J \sigma \mathbf{F}^{-T} d\tilde{x}_3$ (the leading part of the Taylor's expansion).

Note that using the ALE technique with moving mesh, the computed in time-dependent domain G^t velocity \mathbf{v} and pressure p can be presented in the points of the reference domain G , so that, for example, $\mathbf{v}(x, t)$, $x \in G^t$, is presented in the points (\hat{x}, t) , where $x - \hat{x} = \mathbf{u}(\hat{x}, t)$ is the displacement of the point \hat{x} .

The direct COMSOL computations of this model often demonstrate bad convergence. It is explained as follows. COMSOL uses the implicit numerical schemes, and for each time step, it needs to solve a big algebraic nonlinear system of equations. The solver is based on Newton method, which is very sensitive to the choice of the initial approximation. That is why we solve the FSI problem in two steps: first, we solve the Navier–Stokes equations (1) with nonmoving wall, i.e. in the domain G with initial condition (2) and boundary conditions (3) on Γ_2 and (4) on Γ_3 , while the boundary conditions on Γ_1 are replaced by $\mathbf{v} = 0$, $x \in \Gamma_1$. Then, at the second step, the FSI problem is solved using the initial approximations from the first step. This approach improves the convergence of the solver.

In COMSOL simulations, the nonlinear numerical schemes are solved by Newton method (called in COMSOL “automatic”) with PARDISO (direct parallel sparse solver) as solver for linear algebraic systems of equations. We adjusted the time step, event tolerance, step growth rate, BDF (backward differential formula) order, and other parameters for the nonlinear controller to enhance the implicit solver’s convergence.

2 Results

We possess data concerning two distinct patients diagnosed an AF: we denote these as PATIENT A (with “chicken wing” geometry), who had a stroke, and PATIENT B (with “windsock” geometry), who has not got a stroke. After the stroke, PATIENT A recovered

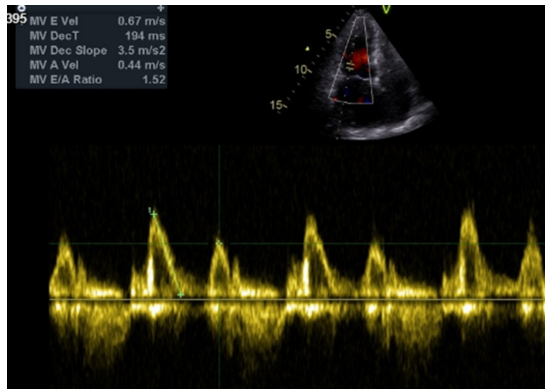


Figure 7. Blood flow through mitral valve during sinus rhythm (PATIENT A specific data).

to sinus rhythm, and then the blood flow velocity through mitral valve was measured by Doppler technique; see Fig. 7. We utilize this graph to prescribe the average velocity $F(t)$ in boundary condition (3); see Fig. 4(b).

Given the inherent limitations in capturing *in vivo* blood velocity measurements within LAA, we are able to compute the magnitude of blood velocity within this area. We validate our simulations comparing the computed normal velocity at the inlet point of the LAA, known as the ostium, with the measured one.

Figure 8 shows the similar order of the normal velocity at the ostium of LAA (AF case), i.e. Doppler measurements are compared to the computer simulations. One notices the peaks of the normal velocity from -0.6 to 0.2 m/s in Doppler measurements compared to the peaks from -0.6 to 0.1 m/s in computations. The error can be explained by a high gradient of solution at the point of measurement.

For each of two patients, we fix three points in the LAA: one at the inlet to the LAA (ostium), one in the middle of the LAA (center), and one near the wall (lateral). Figures 9–11 present the results of computer simulations (velocity magnitude) for the LAA of PATIENT A in case of AF with a rigid (not moving) wall on the left and with FSI (moving wall) on the right. Figures 12–14 present analogous simulations for the LAA of the PATIENT A in the case of sinus rhythm. Figures 15–17 show the graphs of the velocity magnitude for the LAA of PATIENT B in case of AF, and, finally, Figs. 18–20 present the velocity magnitude for the LAA of PATIENT B in case of sinus rhythm. All above-mentioned pictures show the satisfactory stabilization of the velocity to a periodic regime after three heartbeats. These pictures show that in the case of PATIENT A (the one with a stroke), the magnitude order is similar for the rigid wall and FSI computations in the case of AF, but differs significantly for the sinus rhythm, while for the PATIENT B (the one without a stroke), the magnitude order is the same in both AF and sinus rhythm cases. It shows that, probably, the mobility of the wall is more important for the geometry of LAA of the PATIENT A (who had a stroke) than for the geometry of the PATIENT B (who had not). Thus, hypothetically, one can use the comparison of the rigid wall and FSI simulations for AF and sinus rhythm cases to evaluate the type of geometry with a higher

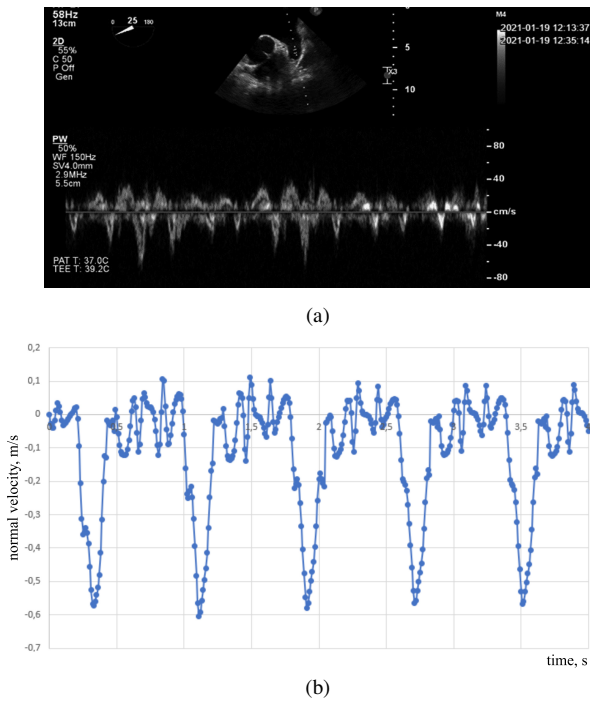


Figure 8. Validation of normal blood velocity at the LAA ostium of PATIENT A: (a) measured; (b) computed.

risk of stroke. Another guess can be done for the case of AF simulations: the magnitudes of the velocity in the LAA are similar for the rigid wall computations and for the FSI model. Note that the rigid wall simulations are much simpler and less time-consumable than FSI.

As we can see on Fig. 21, PATIENT A had in LAA velocity magnitude, which is obviously lower than PATIENT’s B. So, the lower velocity magnitude corresponds to the higher risk of thrombi formation. Notice that PATIENT A has “chicken wing” LAA geometry, while PATIENT B has “windsock” LAA geometry. It shows that the prediction of the stroke via the CFD simulations of the blood flow in the LA may be more realistic than the statistical evaluation based on the classification of the morphology of the LAA.

Finally, the comparison of the computations for sinus rhythm and atrial fibrillation for rigid wall and for FSI allows to conclude the following remarks. For the atrial fibrillation cases, the rigid wall simulations catch the orders of the velocity but not the peaks appearing in the FSI computations due to the wall activity. For the sinus rhythm simulations, the difference of velocities is more significant: approximately two times in Figs. 12–14 (patient a who had a stroke). However, for PATIENT B the computations with rigid wall and FSI for sinus rhythm give similar orders of velocities (regardless some peaks in FSI simulations). It may be explained by the fact that the geometry of the LAA of PATIENT B is less sensitive to the wall activity, and it helps to avoid the stroke.

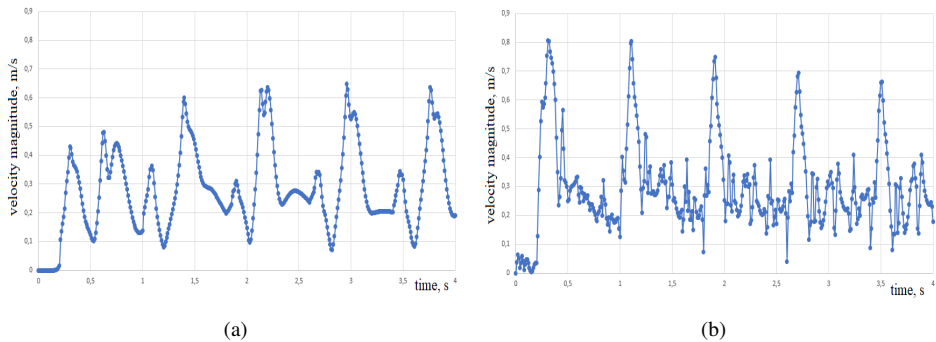


Figure 9. (a) The velocity magnitude at the ostium of LAA of the PATIENT A during atrial fibrillation computed with rigid (not moving) wall; (b) the velocity magnitude at the ostium of LAA of the PATIENT A during atrial fibrillation computed with moving wall (FSI).

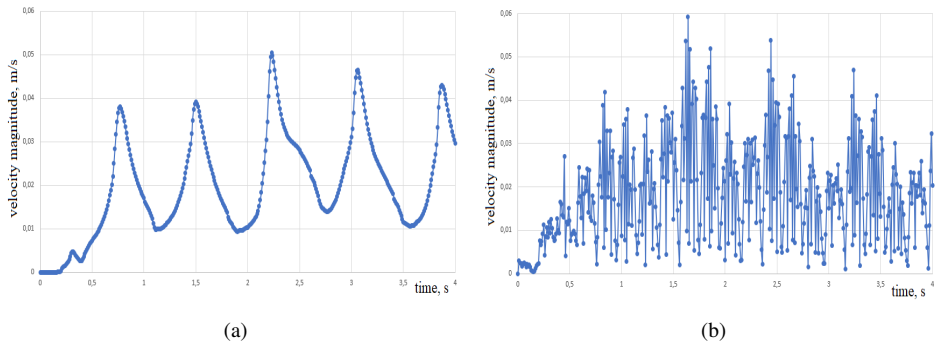


Figure 10. (a) The velocity magnitude at the center of LAA of the PATIENT A during atrial fibrillation computed with rigid (not moving) wall; (b) the velocity magnitude at the center of LAA of the PATIENT A during atrial fibrillation computed with moving wall (FSI).

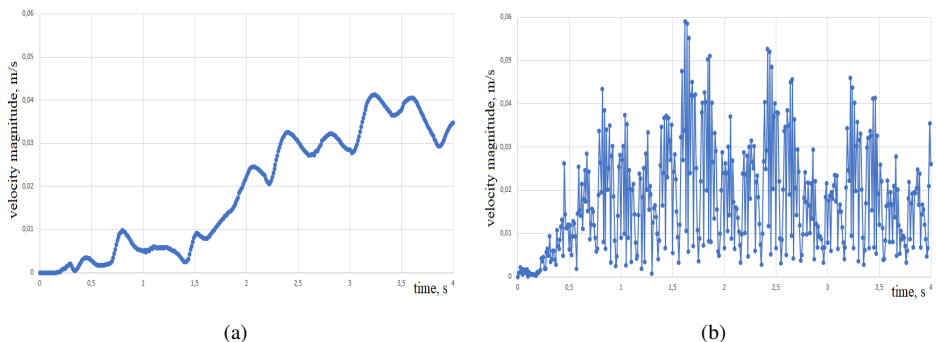


Figure 11. (a) The velocity magnitude at the lateral part of LAA of the PATIENT A during atrial fibrillation computed with rigid (not moving) wall; (b) the velocity magnitude at the lateral part of LAA of the PATIENT A during atrial fibrillation computed with moving wall (FSI).

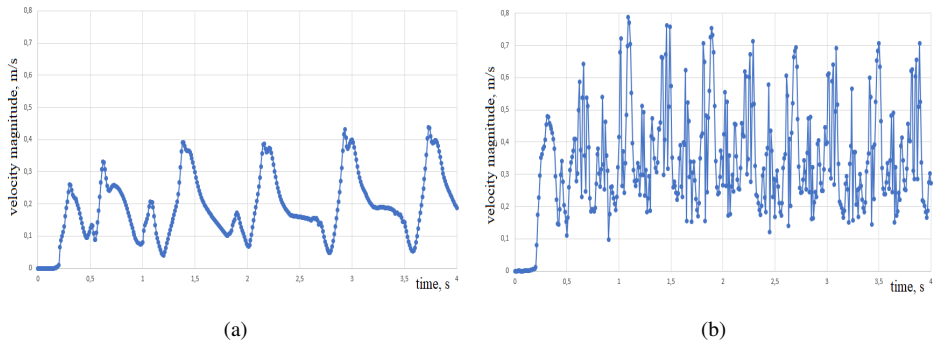


Figure 12. (a) The velocity magnitude at the ostium of LAA of the PATIENT A during sinus rhythm computed with rigid (not moving) wall; (b) the velocity magnitude at the ostium of LAA of the PATIENT A during sinus rhythm computed with moving wall (FSI).

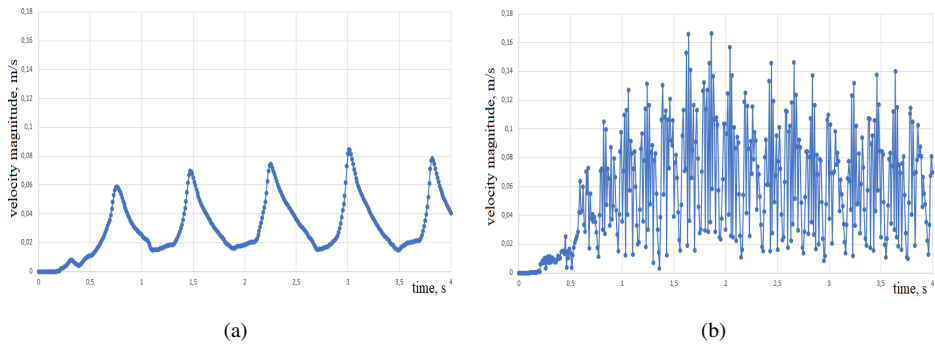


Figure 13. (a) The velocity magnitude at the center of LAA of the PATIENT A during sinus rhythm computed with rigid (not moving) wall; (b) the velocity magnitude at the center of LAA of the PATIENT A during sinus rhythm computed with moving wall (FSI).

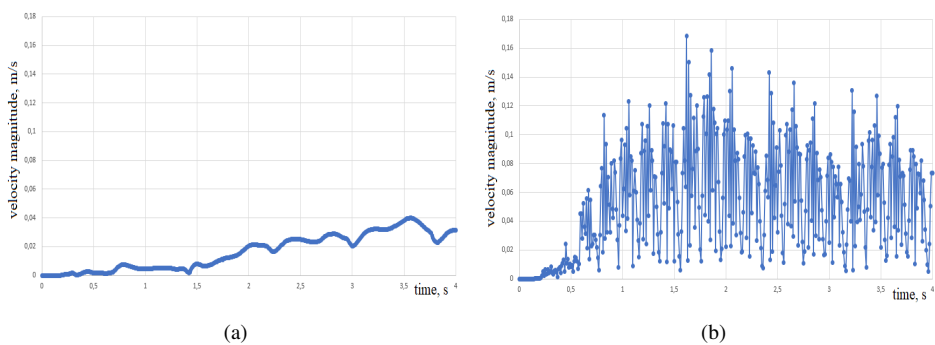


Figure 14. (a) The velocity magnitude at the lateral part of LAA of the PATIENT A during sinus rhythm computed with rigid (not moving) wall; (b) the velocity magnitude at the lateral part of LAA of the PATIENT A during sinus rhythm computed with moving wall (FSI).

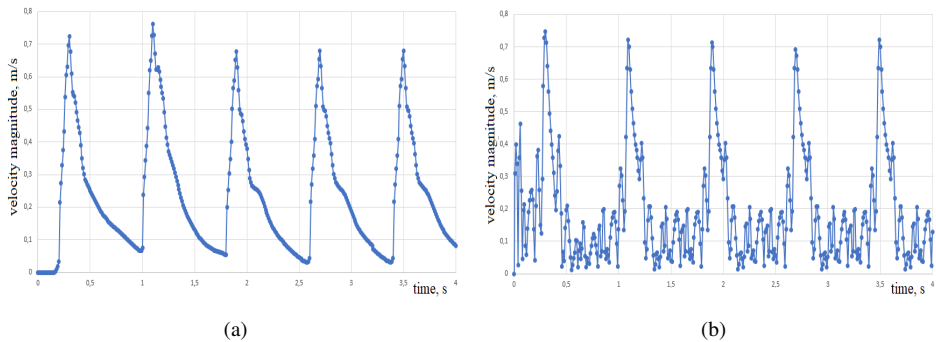


Figure 15. (a) The velocity magnitude at the ostium of LAA of the PATIENT B during atrial fibrillation computed with rigid (not moving) wall; (b) the velocity magnitude at the ostium of LAA of the PATIENT B during atrial fibrillation computed with moving wall (FSI).

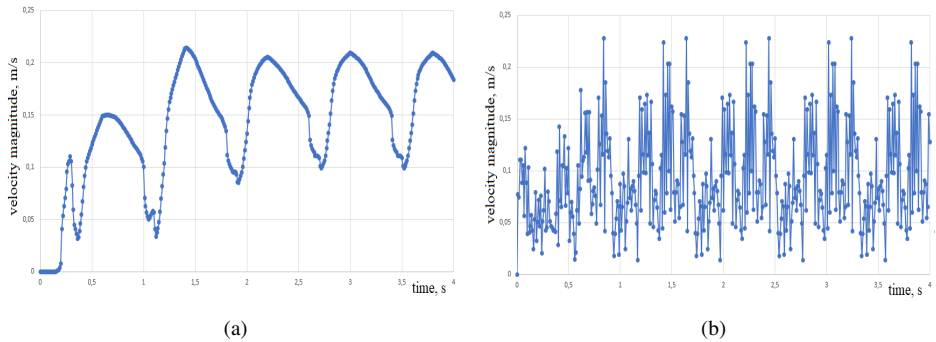


Figure 16. (a) The velocity magnitude at the center of LAA of the PATIENT B during atrial fibrillation computed with rigid (not moving) wall; (b) the velocity magnitude at the center of LAA of the PATIENT B during atrial fibrillation computed with moving wall (FSI).

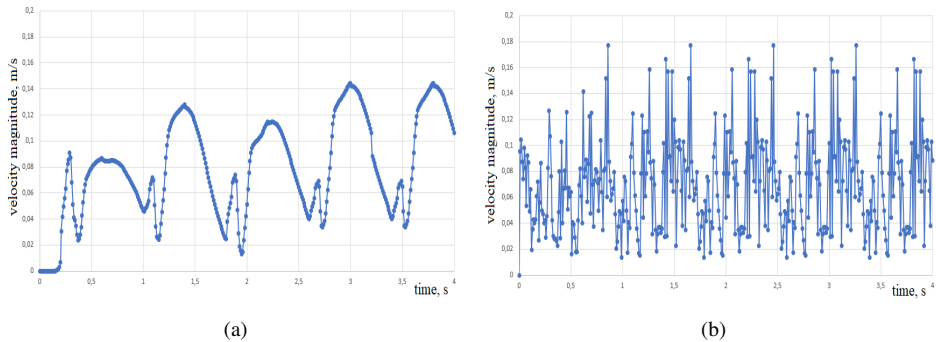


Figure 17. (a) The velocity magnitude at the lateral part of LAA of the PATIENT B during atrial fibrillation computed with rigid (not moving) wall; (b) the velocity magnitude at the lateral part of LAA of the PATIENT B during atrial fibrillation computed with moving wall (FSI).

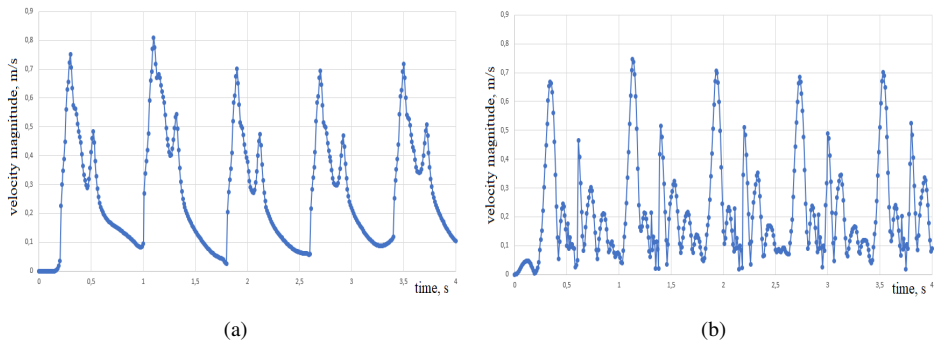


Figure 18. (a) The velocity magnitude at the ostium of LAA of the PATIENT B during sinus rhythm computed with rigid (not moving) wall; (b) the velocity magnitude at the ostium of LAA of the PATIENT B during sinus rhythm computed with moving wall (FSI).

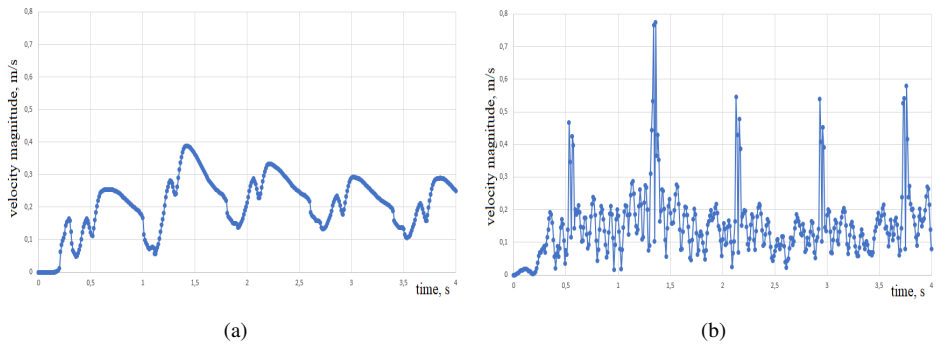


Figure 19. (a) The velocity magnitude at the center of LAA of the PATIENT B during sinus rhythm computed with rigid (not moving) wall; (b) the velocity magnitude at the center of LAA of the PATIENT B during sinus rhythm computed with moving wall (FSI).

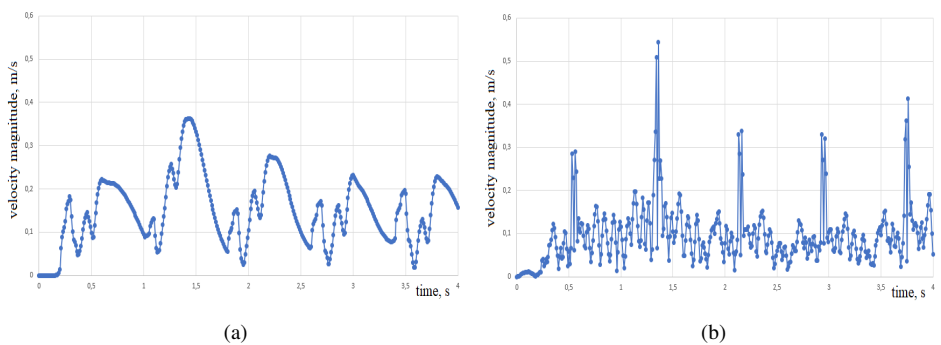


Figure 20. (a) The velocity magnitude at the lateral part of LAA of the PATIENT B during sinus rhythm computed with rigid (not moving) wall; (b) the velocity magnitude at the lateral part of LAA of the PATIENT B during sinus rhythm computed with moving wall (FSI).

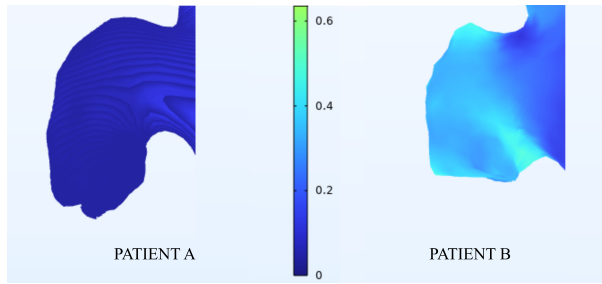


Figure 21. Computed blood flow velocity magnitude (m/s) in the LAA (deep blue color corresponds to a lower velocity magnitude, while light blue corresponds to a higher velocity).

3 Discussion

The present paper tests the FSI approach for the computations of the blood flow in the LA of the heart in cases of an atrial fibrillation and in case of a sinus rhythm. Compared to the existing simulations with rigid motionless heart wall, this approach is more accurate, especially in the case of the sinus rhythm. Compared to the given heart wall velocity approach, the FSI eventually allows obtaining information about the stress-strain state of the heart wall. In the FSI approach, the variation of the Young's modulus of the heart wall during the contraction is very important, and it was taken into consideration in the model. It was pointed out that the two-step COMSOL computations using the rigid wall as the initial approximation for parameters efficiently improves the stability of the computations. The tests were provided for the real-life patient specific geometries of the heart. Although the number of tested cases was modest (two patients), the simulations allowed to adjust the parameters of the model and validate comparing the order of the computed and Doppler-measured velocities in a point of LA, where in-vivo measurements are possible. These results give possibility to pass to more important number of patient specific tests in a forthcoming study in order to find the correlation between the order of the velocity in the parts of LAA and stroke cases of patients. In future studies, the stress-strain state of the heart wall will also be studied.

4 Conclusions

An FSI model of the blood flow in patient-specific LA is introduced. The simulations including the imaging, segmentation, cleaning (noise reduction), domain generation, and FSI computational fluid dynamics within patient-specific LA are provided. The validation of the model is carried out by comparison with the Doppler measurements at the ostium of the LAA. The correlation of the presence of stagnation zones in LAA with the stroke risk is studied. The COMSOL simulations of the FSI model are quite challenging and often the direct application of the code leads to the fail of the convergence. It is pointed out that the two-step computation (rigid wall at the first step and FSI at the second step) improves the convergence of the latter code.

In order to calculate the interaction between the elastic heart wall and blood flow, the mutual effect of the wall and blood in real time, i.e. fully coupled physical interfaces, must be taken into account. Another novelty of the model is the introduction of the time-dependent Young modulus of the heart wall tissue. Indeed, the experimental studies [9] show that the Young modulus of the contracted heart tissue may be ten time higher than the Young modulus of the tissue in relaxed state. Taking into consideration this change in the state of the tissue during contraction is crucial for the FSI model. To stabilize the computations, a wide range of minimum and initial damping factors, along with a fixed recovery damping factor, was used. The potential improvements of the solver stability will correspond to the optimization of the time step, event tolerance, step growth rate, BDF (Backward Differentiation Formula) order, and other parameters for the nonlinear controller to enhance the implicit solver's convergence.

Conflicts of interest. The authors declare no conflicts of interest.

Acknowledgment. G. Panasenko is grateful to Olga Štikonienė for useful discussions. The authors are grateful to Sofija Marija Everatt for the help with imaging, cleaning, and making geometry.

Appendix: Software details

The .stl file format is used in medical cardiac scanning equipment. Typically, it contains scanning errors that resemble geometric peaks. We clean the geometry and transform it into .step format by using a specialized program Meshlab. The CAD module built in Comsol is used to import the corrected and augmented geometry into the physical module. We use a multiphysics interface known as fluid-structure interaction (FSI) in this study. The shell interface of thin structures is used for structural analysis computations. The heart wall was modeled as an elastic material with changing in time Young's modulus and finite strains. In laminar flow physics, the hemodynamical model of blood flow is chosen. The inflow and outflow boundary conditions used the fully developed flow option corresponding to the nonstationary Poiseuille flow. The given incoming flow is shared between four pulmonary veins so that the average velocity is the same for all inlets. By applying the boundary condition "Suppress Backflow" on the outlet, the mitral valve's operation was approximated and synchronized with the inlets' function. In order to simulate the deformations of the heart wall during the computation and approximating the muscular tissue around it, we employ a time-varying external normal wall pressure function. Time stepping was carried out using the implicit time-dependent solver algorithms, which uses variable-order variable-step-size Backward Differentiation Formulas (BDF). A direct PARDISO linear solver and a Newtonian nonlinear method with a large range of damping factors were used to solve the numerical scheme at each time step. The physics controlled mesh with a normal element size is generated. It has tetrahedric elements for the fluid part and triangular elements matching the fluid domain tetrahedrons. The final mesh contains: 7324 tetrahedrons for PATIENT A and 6683 ones for PATIENT B.

References

1. M. Anand, K. Rajagopal, K.R. Rajagopal, A model for the formation and lysis of blood clots, *Pathophysiol. Haemost. Thromb.*, **34**(2–3):109–120, 2006, <https://doi.org/10.1159/000089931>.
2. G.M. Bosi, A. Cook, R. Rai, L.J. Menezes, S. Schievano, R. Torii, G. Burriesci, Computational fluid dynamics analysis of the left atrium appendage to predict thrombosis risk, *Front. Cardiovasc. Med.*, **5**:34, 2018, <https://doi.org/10.3389/fcvm.2018.00034>.
3. A. Bouchnita, A. Tosenberger, V. Volpert, On the regimes of blood coagulation, *Appl. Math. Lett.*, **51**:74–79, 2016, <https://doi.org/10.1016/j.aml.2015.07.010>.
4. L. Di Biase et al., Does the left atrial appendage morphology correlate with the risk of stroke in patients with atrial fibrillation? results from a multicenter study, *J. Am. Coll. Cardiol.*, **60**:531–538, 2012, <https://doi.org/10.1016/j.jacc.2012.04.032>.
5. S.S. Virani et al., Heart disease and stroke statistics—2021 update: A report from the American Heart Association, *Circulation*, **143**(8):e254–e743, 2021, <https://doi.org/10.1161/CIR.0000000000000950>.
6. A.L. Fogelson, Cell-based models of blood clotting, in A.R.A. Anderson, M.A.J. Chaplain, K.A. Rejniak (Eds.), *Single-Cell-Based Model in Biology and Medicine*, Math. Biosci. Interact., Birkhäuser, Basel, 2007, pp. 243–269, https://doi.org/10.1007/978-3-7643-8123-3_11.
7. A.L. Fogelson, R.D. Guy, Platelet-wall interactions in continuum models of platelet thrombosis: Formulation and numerical solution, *Math. Med. Biol.*, **21**(4):293–334, 2004, <https://doi.org/10.1093/imammb21.4.293>.
8. M. García-Villalba, L. Rossini, A. Gonzalo, D. Vigneault, P. Martinez-Legazpi, E. Duran, O. Flores, J. Bermejo, E. McVeigh, A.M. Kahn, J.C. del Álamo, Demonstration of patient-specific simulations to assess left atrial appendage thrombogenesis risk, *Front. Physiol.*, **12**:596, 2021, <https://doi.org/10.3389/fphys.2021.596596>.
9. J.D. Humphrey, Continuum mechanics of soft tissues, *Proc. R. Soc. Lond., Ser. A.*, **459**:3–46, 2003, <https://doi.org/10.1098.1060>.
10. S.W. Jordan, E.L. Chaikof, Simulated surface-induced thrombin generation in a flow field, *Biophys. J.*, **101**:276–286, 2011, <https://doi.org/10.1016/j.bpj.2011.05.056>.
11. H. Kamel, P. M. Okin, M. Elkind, C. Iadecola, Atrial fibrillation and mechanisms of stroke: Time for a new model, *Stroke*, **47**(3):895–900, 2016, <https://doi.org/10.1161/STROKEAHA.115.012004>.
12. N. Karim, S.Y. Ho, E. Nicol, W. Li, F. Zemrak, V. Markides, V. Reddy, T. Wong, The left atrial appendage in humans: structure, physiology, and pathogenesis, *Europace*, **22**(1):5–18, 2020, <https://doi.org/10.1093/europace/euz212>.
13. A.I. Lobanov, T.K. Starozhilova, The effect of convective flows on blood coagulation processes, *Pathophysiol. Haemost. Thromb.*, **34**(2–3):121–134, 2005, <https://doi.org/10.1159/000089932>.
14. A. Masci, L. Barone, L. Dedè, M. Fedele, C. Tomasi, A. Quarteroni, C. Corsi, The impact of left atrium appendage morphology on stroke risk assessment in atrial fibrillation: A computational fluid dynamics study, *Front. Physiol.*, **9**:19–38, 2019, <https://doi.org/10.3389/fphys.2018.01938>.

15. P.K. Mason, D.E. Lake, J.P. Dimarco, J.D. Ferguson, J.M. Mangrum, K.C. Bilchick, L.P. Moorman, J.R. Moorman, Impact of the CHA₂DS₂-VASc score on anticoagulation recommendations for atrial fibrillation, *Am. J. Med.*, **125**(6):603–606, 2012, <https://doi.org/10.1016/j.amjmed.2011.09.030>.
16. K. Pileckas, Existence of solutions with the prescribed flux of the Navier–Stokes system in an infinite cylinder, *J. Math. Fluid Mech.*, **8**(4):542–563, 2006, <https://doi.org/10.1007/s00021-005-0187-1>.
17. K. Pileckas, V. Keblikas, On the existence of the nonstationary Poiseuille solution, *Sib. Math. J.*, **46**(3):514–526, 2005, <https://doi.org/10.1007/s11202-005-0053-7>.
18. E.A. Pogorelova, A.I. Lobanov, Influence of enzymatic reactions on blood coagulation auto-wave, *Biophysics*, **59**(1):110–118, 2014, <https://www.doi.org/10.1134/S0006350914010151>.
19. A. Tokarev, G. Panasenko, F. Ataullakhanov, Segregation of flowing blood: Mathematical description, *Math. Model. Nat. Phenom.*, **6**(5):281–319, 2011, <https://doi.org/10.1051/mmnp/20116511>.
20. A. Tokarev, I. Sirakov, G. Panasenko, V. Volpert, E. Shnol, A. Butylin, F. Ataullakhanov, Continuous mathematical model of platelet thrombus formation in blood flow, *Russ. J. Numer. Anal. Math. Model.*, **27**(2):192–212, 2012, <https://doi.org/10.1051/mmnp/2008007>.
21. A.A. Tokarev, Yu.V. Krasotkina, M.V. Ovanesov, M.A. Panteleev, M.A. Azhigirova, V.A. Volpert, F.I. Ataullakhanov, A.A. Butilin, Spatial dynamics of contact-activated fibrin clot formation in vitro and in silico in haemophilia B: Effects of severity and Ahemphil B treatment, *Math. Model. Nat. Phenom.*, **1**(2):124–137, 2006, <https://doi.org/10.1051/mmnp/2008007>.
22. A. Tosenberger, F. Ataullakhanov, N. Bessonov, M. Panteleev, A. Tokarev, V. Volpert, Modelling of thrombus growth inow with a dpd-pde method, *J. Theor. Biol.*, **337**:30–41, 2013, <https://doi.org/10.1016/j.jtbi.2013.07.023>.
23. A. Tosenberger, F. Ataullakhanov, N. Bessonov, M. Panteleev, A. Tokarev, V. Volpert, Modelling of platelet-fibrin clot formation in flow with a DPD-PDE method, *J. Math. Biol.*, **72**(3):649–681, 2015, <https://doi.org/10.1007/s00285-015-0891-2>.
24. S. Valvez, M. Oliveira-Santos, A.P. Pledade, L. Goncalves, A.M. Amaro, Computational flow dynamic analysis in left atrium appendage thrombus formation risk: A review, *Appl. Sci.*, **13**(14):8201, 2023, <https://doi.org/10.3390/app13148201>.
25. D. Vella, A. Monteleone, G. Musotto, G.M. Bosi, G. Burriesci, Effect of the alternations in contractility and morphology produced by atrial fibrillation on the thrombosis potential of the left atrial appendage, *Front. Bioeng. Biotechnol.*, **26**(9):586041, 2021, <https://doi.org/10.3389/fbioe.2021.586041>.
26. Z. Xu, N. Chen, M.M. Kamocka, E.D. Rosen, M. Alber, A multiscale model of thrombus development, *J. R. Soc. Interface*, **5**(24):705–722, 2008, <https://doi.org/10.1098/rsif.2007.1202>.
27. A. Yazdani, H. Li, J.D. Humphrey, G.E. Karniadakis, A general shear-dependent model for thrombus formation, *PLoS Comput. Biol.*, **13**(1):e1005291, 2017, <https://doi.org/10.1371/journal.pcbi.1005291>.